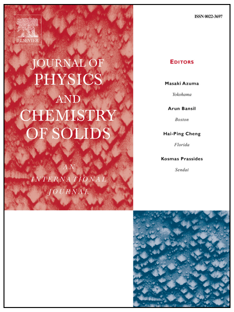

Synthesis and characterization of novel Ag/ZnO nanoparticles for photocatalytic degradation of methylene blue under UV and solar irradiation

M.F. Abdel Messih, M.A. Ahmed, Ayman Soltan, Samy Sobhy Anis

PII: S0022-3697(19)30210-0

DOI: https://doi.org/10.1016/j.jpcs.2019.109086

Article Number: 109086

Reference: PCS 109086

To appear in: *Journal of Physics and Chemistry of Solids*

Received Date: 27 February 2019

Revised Date: 30 June 2019

Accepted Date: 1 July 2019

Please cite this article as: M.F.A. Messih, M.A. Ahmed, A. Soltan, S.S. Anis, Synthesis and characterization of novel Ag/ZnO nanoparticles for photocatalytic degradation of methylene blue under UV and solar irradiation, *Journal of Physics and Chemistry of Solids* (2019), doi: https://doi.org/10.1016/j.jpcs.2019.109086.

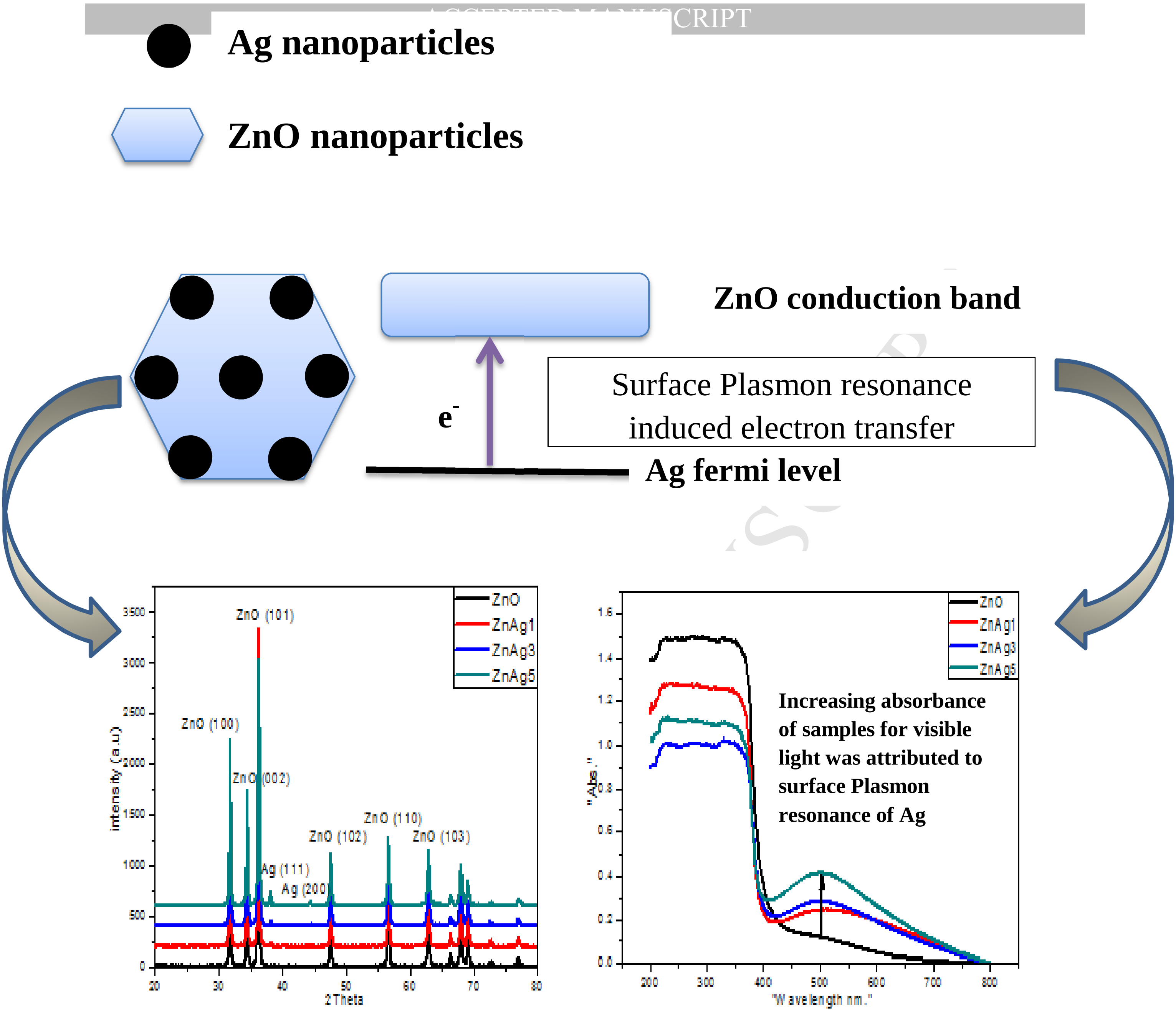

Surface Plasmon resonance induced electron transfer

Increasing absorbance of samples for visible light was attributed to surface Plasmon resonance of Ag

Synthesis and characterization of novel Ag/ZnO nanoparticles for photocatalytic degradation of methylene blue under UV and solar irradiation

M.F. Abdel Messih, M.A. Ahmed*, Ayman Soltan, Samy Sobhy Anis

Chemistry Department, Faculty of Science, Ain Shams University, Egypt

Abstract

ZnO containing various proportions of metallic silver nanoparticles (0–5 wt% Ag) were synthesized by a combined sol-gel and chemical reduction method in which chitosan acts as a steric stabilizer and environmentally benign reducing agent for silver ions. Structural, morphological, textural, and optical properties of the prepared nanoparticles were investigated by X-ray diffraction, high-resolution transmission electron microscopy, nitrogen physisorption, diffuse reflectance spectroscopy, and photoluminescence spectroscopy. X-ray diffraction and X-ray photoelectron spectroscopy analyses revealed the successful transformation of silver ions into metallic silver nanoparticles (Ag) and suggest a strong interaction between ZnO and silver metal. Photoluminescence analysis indicated the positive influence of metallic silver in limiting electron-hole recombination. The photocatalytic performance of Ag/ZnO nanoparticles was studied by our following the photodegradation of the dye methylene blue under UV and solar irradiation. The incorporation of an appropriate amount of Ag (3 wt%) enhanced the photocatalytic activity under UV and solar irradiation. The enhancement of photocatalytic reactivity under UV irradiation was attributed to the possible transfer of photogenerated electrons from the ZnO conduction band to the Ag Fermi level, which limits electron-hole recombination and increases the degradation efficiency. However, under solar irradiation, the higher photocatalytic reactivity was attributed to surface plasmon resonance of metallic Ag nanoparticles. Photoluminescence analysis with use of terephthalic acid revealed that incorporation of silver nanoparticles on the ZnO surface was accompanied by an increase in the concentration of hydroxyl radicals, which are considered a main reactive species in dye degradation.

Keywords

Chitosan, Ag-doped ZnO, Surface Plasmon resonance, Methylene blue photocatalytic degradation

1. Introduction

Synthetic dyes are used in various industries, such as the textile industry, the leather tanning industry, and the paper industry. These toxic synthetic dyes are released in significant amounts into the environment, causing water pollution [1]. Photocatalysis is a promising technology for complete destruction of organic pollutants without the formation of secondary pollutants that require further treatment [2]. Various metal oxide semiconductors, such as TiO_2 [3], ZnO [4], and SnO_2 [5], are considered to be promising photocatalysts for complete degradation of organic pollutants to environmentally friendly species [6]. ZnO is a promising semiconductor because of the low cost of its metal precursors, its nontoxicity, and its high photosensitivity [7–10]. However, the high recombination rate of photogenerated electron-hole pairs [11] and the wide band gap [12, 13] are the main drawbacks that limit the industrial use of ZnO nanoparticles. ZnO exhibits low efficiency under solar irradiation because of its wide band gap and rapid electron-hole recombination [9]. Various recent research studies indicate that the introduction of noble metal nanoparticles, such as Pd [14], Pt [15], Au [16], and Ag [17–27], on the ZnO surface enhances the photocatalytic reactivity in degradation of various organic dyes. Among noble metals, metallic silver nanoparticles exhibit high efficiency in enhancing the photocatalytic activity of ZnO because of their appropriate price in comparison with other noble metals such as Au, Pt, and Pd [28]. The enhanced UV-light-driven photocatalytic efficiency was attributed to efficient separation of the photogenerated electrons and holes in the presence of Ag [11, 21, 24,]; however, the higher visible-light-driven photocatalytic efficiency was attributed to surface plasmon resonance of Ag [17, 23, 26, 27]. It is interesting to mention that the existence of an appropriate amount of metallic silver nanoparticles is a major factor in optimizing the photocatalytic reactivity. A small amount of Ag^0 is not sufficient to enhance the reactivity; however, a large amount of silver metal acts as recombination centers that prevent the production of a large amount of radicals and reduce the lifetime of the photocatalyst. The homogeneous dispersion of metallic silver nanoparticles on the ZnO surface requires a mild reduction process; however, most of the previous research work usually used a vigorous reducing agent such as $NaBH_4$, ascorbic acid, or $LiAlH_4$. These strong reducing agents lead to agglomeration of silver nanoparticles on the ZnO surface, which inhibits light penetration and results in the silver nanoparticles acting as recombination centers for the charge carriers. In this work, Ag/ZnO nanoparticles with various amounts of silver (1, 3, and 5 wt%) were prepared by an innovative combined sol-gel and chemical reduction method in which chitosan plays a dual role as a template and a reducing agent. Wei and Qian [28] attributed the reduction of silver ions by chitosan to oxidation of chitosan $OH^{\cdot}$ as shown in Fig. 1. The effect of Ag on the photocatalytic efficiency of ZnO was investigated with methylene blue (MB) as a cationic pollutant model. The results indicate that addition of Ag to the ZnO matrix increases its photocatalytic efficiency. Moreover, a possible mechanism is discussed and suggested.

2. Experimental

2.1. Materials

All the reagents, including zinc nitrate hexahydrate ($Zn(NO_3)_2 \cdot 6H_2O$; purity greater than 99%), silver nitrate ($AgNO_3$; purity greater than 98%), 2-propanol ($(CH_3)_2CHOH$; purity 99.7% or greater), low molecular weight chitosan, glacial acetic acid (CH_3COOH; purity greater than 99%), ammonia solution (NH_4OH; purity 32%), and MB ($C_{16}H_{18}ClN_3S$), were purchased from Sigma-Aldrich.

2.2. Preparation of pure and Ag-doped ZnO

A series of Ag/ZnO samples were prepared by our dissolving 18.22, 18.095, 17.729, and 17.36 g of zinc nitrate in distilled water with 7.87, 23.62, and 39.37 ml of 1% (w/v) $AgNO_3$ to obtain 0, 1, 3, and 5 wt% metallic silver nanoparticles on the ZnO surface (ZnAg1, ZnAg3, and ZnAg5, respectively). Each solution was subjected to vigorous stirring for 1 h, followed by addition of 5 ml of 2% (w/v) chitosan dissolved in glacial acetic acid with constant stirring for another 1 h. Then, drops of ammonia solution were added until a turbid sol formed, which was subsequently converted to a viscous gel. The gel was left to age for 3 days. Finally, the gel was filtered, washed with distilled water, dried at 100 °C, and calcined at 500 °C for 3 h to obtain the desired materials. Pure ZnO was prepared by the same method but without $AgNO_3$.

2.3. Physicochemical characterization of the photocatalysts

X-ray diffractograms of the prepared samples over the 2θ range from 20^o to 100^o were obtained with a Philips X'PERT MPD diffractometer with Ni-filtered Cu Kα radiation (λ = 0.154 nm). The crystallite size of the prepared samples was estimated from the line broadening of the wurtzite (101) peak (2θ = 36.2°) with use of Scherrer's equation.

Micrographs of the samples, from which the size and shape of the particles composing the samples were obtained, were captured by a JEOL 2100 high-resolution transmission electron microscope. The samples for microscopic analysis were dispersed in water by an ultrasonicator and dropped on a carbon-coated copper grid.

Nitrogen adsorption-desorption isotherms (at −196.6 °C) were obtained with a NOVA 3200 surface area and pore size analyzer. Before analysis, all samples were degassed overnight at room temperature.

UV-visible diffuse absorption spectra were recorded with a Shimadzu UV-2600 UV-vis spectrophotometer, from which the band gap energies of the samples were determined by the Tauc method with the following equation [29]: $f(R)h\nu = A(h\nu - E_g)^n$, where f(R) is the so-called Kubelka-Munk function, hν is the incident photon energy, A is an energy-independent constant, E_g is the optical band gap, and n is a constant that determines the type of optical transitions. For a direct allowed transition, n = 1/2, while for an indirect allowed transition, n = 2.

Photoluminescence spectra were recorded with a Lumina fluorescence spectrometer (Thermo Fisher Scientific), from which the electronic band structures of the samples were revealed.

2.4. Photocatalytic activity test

In the photocatalytic reactor shown in Fig. 2, the photoactivity of the samples was investigated through photodegradation of 2×10^{-5} M MB aqueous solution. The photocatalytic degradation of MB over each sample surface was followed by spectrophotometric measurements using the following procedure: In the photocatalytic reactor, 0.1 g of sample was mixed with 100 ml of as aqueous solution of the dye, and the mixture was stirred for 30 min in the dark to obtain adsorption-desorption equilibrium of the dye on the sample surface. After equilibration, the concentration of dye in terms of absorbance was measured with a Thermo Scientific Evolution 300 UV-vis spectrophotometer, and the value was taken as the initial concentration (C_0) of the dye. Then, a mercury UV lamp operating at 365 nm was switched on over the suspension, and at different irradiation time intervals 5 ml of dye solution was withdrawn and analyzed with the UV-vis spectrophotometer to determine the residual concentration (C_t) of the dye. Finally, the percent photocatalytic activity of each sample was calculated by the following equation:

$$\text{Photocatalytic activity (\%)} = [1 - (C_t/C_0)] \times 100.$$

The photocatalytic reactivity of ZnO and ZnAg3 under visible light was estimated with use of a xenon lamp with an intensity of 100 W, and a cutoff filter was used to remove UV radiation ($\lambda \leq 420$ nm).

3. Results and discussion

3.1. Physicochemical characterization

3.1.1. Structural analysis

3.1.1.1. X-ray diffraction

X-ray diffraction (XRD) patterns of ZnO containing various proportions of metallic silver nanoparticles are shown in Fig. 3. As shown in Fig. 3, all samples exhibited diffraction peaks at 2θ = 31.7°, 34.4°, 36.2°, 47.5°, 56.6°, 62.8°, 66.3°, 67.9°, 69.1°, 72.6°, and 76.9°, corresponding, respectively, to the (100), (002), (101), (102), (110), (103), (200), (112), (201), (004), and (202) crystal planes of ZnO wurtzite phase with lattice parameters a = 3.249 Å and c = 5.206 Å (JCPDS card no. 03-065-3411). On careful examination of the XRD patterns, one can notice the existence of three prevailing diffraction peaks, at 2θ = 38.1°, 44.2°, and 64.4°, which correspond to the (111), (200), and (220) crystal planes of Ag metal (JCPDS card no. 00-004-0783). The existence of metallic silver nanoparticles confirms the successful role of chitosan in reducing silver ions to silver nanoparticles. The crystallite sizes of pure and Ag-doped ZnO nanocrystalline powders were determined from the broadening of the

Wurtzite (101) peak (2θ = 36.2°) with use of Scherrer's equation and are given in Table 1. The average crystallite size for all the samples was 55.7 nm, with a standard deviation of 6.5 nm, giving a range of 47.5–61 nm.

3.1.1.2. High-resolution transmission electron microscop

Fig. 4a–d shows **high-resolution transmission electron microscope** images of ZnO, ZnAg1, ZnAg3, and ZnAg5. The images reveal the existence of hexagonal ZnO nanoparticles with size ranging between 32 and 71 nm. It is interesting to notice the homogeneous dispersion of metallic silver nanospheres on the ZnO surface for ZnAg1 and ZnAg3. However, the silver nanoparticles prefer to segregate as a single phase when the silver content is increased to 5 wt%, as the silver nanoparticles seem to form an outer layer coating ZnO particles. For ZnAg3, Fig. 4e shows a d spacing of 0.256, corresponding to the (101) plane of ZnO, and of 0.235, corresponding to the (111) plane of metallic silver nanoparticles,4 and illustrates the hybrid interaction between Ag^0 on ZnO nanoparticles

3.1.2. Textural analysis by the nitrogen physisorption method

Fig. 5 shows N_2 adsorption–desorption isotherms of ZnO, ZnAg1, ZnAg3, and ZnAg5. According to IUPAC [30], the adsorption isotherms are classified as type III, exhibiting an H3 hysteresis loop that arises from the existence of slit-like mesopores. A type III isotherm is a characteristic of weak gas-solid interactions that cause the uptake at low relative pressures to be small; but once a gas molecule has become adsorbed, the adsorbate-adsorbate forces will promote the adsorption of further gas molecules—a cooperative process—so the isotherms will become convex to the pressure axis. Thus in systems that give rise to a type III isotherm, the multilayer is being built up on some parts of the surface, while the monolayer is still incomplete on other parts. The incorporation of 1 and 3 wt% Ag is accompanied by a reduction in sample porosity due to deposition of metallic silver nanoparticles inside the pore structure, and the two samples seems to be completely nonporous. However, an increase in silver content is accompanied by separation of metallic silver nanoparticles as a separate phase, and the ZnO nanoparticles retain their porosity. The surface area calculated by the Brunauer-Emmett-Teller equation and the pore volume and pore diameter estimated by the Barrett-Joyner-Halenda method are given in Table 1. The specific surface area ranges between 4 and 7.2 m^2/g, influenced by the amount of silver in each sample. Consequently, use of the Brunauer-Emmett-Teller equation is not the most suitable method for evaluation of the monolayer capacity and specific surface area of solids with a type III isotherm.

3.1.3. X-ray photoelectron spectroscopy analysis

The surface elemental composition and the surface oxidation state of Zn, O, and Ag of ZnAg5 nanoparticles were analyzed by X-ray photoelectron spectroscopy (XPS). It is evident from the full survey spectrum presented in Fig. 6 that the sample contains three elements—Zn, O, and Ag—confirming the sample purity. In the spectra obtained, Zn was identified through its characteristic two fitted peaks at binding energies of 1020 and 1043 eV, corresponding to Zn $2p_{3/2}$ and Zn $2p_{1/2}$, respectively, representing the existence of the Zn^{2+} oxidation state. Lattice oxygen in ZnO was detected through its specific Gaussian-fitted peak located at a binding energy of 529.5 ± 0.2 eV. In Fig. 6c the peaks at 367 and 373 eV are attributed to Ag $3d_{5/2}$ and Ag $3d_{3/2}$, respectively, corresponding to metallic silver (Ag^0) [1–3]. The peaks for bulk silver slightly shifted to lower binding energy reported in the literature (368.2 for Ag $3d_{5/2}$ and 374.2 for Ag $3d_{3/2}$) are attributed to the strong interaction between ZnO and metallic silver nanoparticles and electron transfer between the ZnO conduction band (CB) and the metallic silver nanoparticles [31–33].

<u>3.1.4. Optical analysis</u>

<u>3.1.4.1. Diffuse reflectance spectra</u>

The absorption spectra for ZnO containing various proportions of metallic silver nanoparticles are illustrated in Fig. 7, showing a strong absorption edge in the UV region (200–400 nm) due to charge-transfer absorption from the valence band (VB) to the CB of ZnO. Incorporation of metallic silver nanoparticles was associated with a shift of the photocatalytic response to the visible region. In particular, ZnAg5 exhibited the highest absorption edge in the visible region because of the surface plasmon absorption of Ag [34]. As seen in Fig. 8, the band gap energy (E_g) of the samples was determined from the $(Ah\nu)^2$ versus photon energy ($h\nu$) plot through the intercept of its linear region with the x-axis (Table 2). E_g for pure ZnO was 3.22 eV, and on doping with Ag metal, the band gap energy was reduced to 3.18 eV, which causes a shift of the absorption edge to longer wavelength.

3.1.4.2. Photoluminescence spectra

Fig. 9 shows the photoluminescence spectra of ZnO and ZnAg3 for an excitation wavelength of 325 nm. For ZnO, the presence of two bands, at 333 and 390 nm, due to band edge emission and defect-related emission, respectively [35], is clearly observed. The pronounced reduction in photoluminescence intensity on introduction of metallic silver nanoparticles was attributed to a decrease in the electron-hole recombination rate [36-37].

3.2. Photocatalytic degradation of MB over pure and Ag-doped ZnO

3.2.1. Kinetics of MB degradation

Fig. 10 illustrates the photocatalytic degradation of MB over ZnO photocatalysts containing various proportions of metallic silver nanoparticles after 240 min of UV irradiation with a catalyst loading of 0.1 g/100 ml. The degradation of MB was evaluated by our following the gradual reduction of intensity of the maximum absorption peak at 664 nm with time. To estimate the photocatalytic reactivity of the samples with regard to degradation of of MB, catalytic parameters such as the percent photocatalytic activity and turnover rate (number of moles converted or produced per gram of photocatalyst per unit time) were calculated (Table 3). Two facts can be extracted from the results in Table 3: the first is the low photocatalytic activity and turnover rate of ZnO, which can be attributed to electron-hole recombination; the second is the increase in ZnO photocatalytic activity and turnover rate on silver doping, which can be attributed to the transfer of photogenerated electrons from the ZnO CB to silver nanoparticles, which limits electron-hole recombination [38–42].

Fig. 11 illustrates the first-order kinetics for MB degradation [43–45]:

$$\ln C_t = \ln C_0 - kt.$$

The rate constant, k, was estimated from the slope of the straight line of the ln C_t versus time plot. Moreover, the half-life, $t_{1/2}$, can be calculated from the following equation:

$$t_{1/2} = \ln 2/k.$$

The kinetic parameters are listed in Table 4. The rate constants follow the sequence ZnAg3 > ZnAg5 > ZnAg1 > ZnO, in agreement with the results for percent photocatalytic activity.

The results reported in Section 3.1.3.1 indicated that incorporation of metallic silver nanoparticles shifted the photocatalytic response to visible light. Consequently, to ascertain the capability of Ag/ZnO nanocomposites for photodegradation of organic pollutants in the visible region, photocatalytic degradation of MB over ZnAg3 under solar irradiation was studied. From Fig. 12, 96% of MB was removed, and by our taking into account the 40% photolysis of MB, ZnAg3 was found to remove 56% of MB by photodegradation under solar irradiation.

3.2.2. The proposed mechanism for Ag/ZnO photocatalytic activity

3.2.2.1. Under UV irradiation

The photocatalytic process under UV irradiation for Ag/ZnO can be investigated by the following suggested mechanism (as shown in Fig. 13). On exposure of ZnO nanoparticles to UV light with energy higher than or equal to the band gap energy, an electron (e^-) from the VB is transferred to the CB, creating a hole (h^+) in the VB (Eq. 1) [39, 41, 46–49]. Then, the photogenerated electrons in the ZnO CB are transferred to the Fermi level of silver nanoparticles (Eq. 2), which is energetically favorable and suppresses electron-hole recombination. Then Ag trapped electrons and ZnO trapped holes react with the preadsorbed oxygen (Eq. 3) and surface-bound hydroxyl groups (–OH) (Eq. 4), respectively, to generate hydroxyl radicals. Finally the hydroxyl radicals degrade MB by hydrogen abstraction and subsequent oxidation processes (Eq. 5) [35].

$$\mathrm{ZnO} + h\nu\ (\mathrm{UV}) \rightarrow h_{VB}^{+} + e_{CB}^{-} \qquad (1)$$

$$\mathrm{ZnO}\ (e_{CB}^{-}) + \mathrm{Ag} \rightarrow \mathrm{ZnO}-\mathrm{Ag}\ (e^{-}) \qquad (2)$$

$$\mathrm{ZnO}-\mathrm{Ag}\ (e^{-}) + O_2 \rightarrow \mathrm{ZnO}-\mathrm{Ag} + O_2^{\bullet -} \xrightarrow{H^+} 2HO_2^{\bullet} \rightarrow H_2O_2 \xrightarrow{O_2^{\bullet -}} {}^{\bullet}OH + OH^{-} + O_2 \qquad (3)$$

$$\mathrm{ZnO}\ (h_{VB}^{+}) + OH^{-} \rightarrow \mathrm{ZnO} + {}^{\bullet}OH \qquad (4)$$

$$\mathrm{MB} + {}^{\bullet}OH \rightarrow H_2O + \mathrm{MB}^{+\bullet} \rightarrow \text{degradation products} \qquad (5)$$

3.2.2.2. Under solar irradiation

The photocatalytic process under solar irradiation for Ag/ZnO can be understood by the following suggested mechanism (as shown in Fig. 14). On exposure of silver nanoparticles to solar irradiation, electron-hole pairs are generated as a result of absorption of visible light through surface plasmon resonance (Eq. 6). Then the plasmon-induced electrons of silver nanoparticles are quickly injected into the ZnO CB (Eq. 7). Then ZnO trapped electrons and Ag trapped holes react with the preadsorbed oxygen (Eq. 8) and surface-bound hydroxyl groups (–OH) (Eq. 9), respectively, to generate hydroxyl radicals. Finally, the hydroxyl radicals degrade MB by hydrogen abstraction and subsequent oxidation processes (Eq. 5) [11, 17]. Consequently, Ag/ZnO nanocomposite samples appear to have different electron transfer directions under UV irradiation and solar irradiation.

$$\mathrm{Ag} + h\nu\ (\text{visible light}) \rightarrow h^{+} + e^{-} \qquad (6)$$

$$\mathrm{Ag}\ (e^{-}) + \mathrm{ZnO} \rightarrow \mathrm{ZnO}\ (e_{CB}^{-}) + \mathrm{Ag}\ (h^{+}) \qquad (7)$$

$$\mathrm{ZnO}\ (e_{CB}^{-}) + O_2 \rightarrow \mathrm{ZnO} + O_2^{\bullet -} \xrightarrow[H^+]{} 2HO_2^{\bullet} \rightarrow H_2O_2 \xrightarrow[O_2^{\bullet -}]{} {}^{\bullet}OH + OH^{-} + O_2 \qquad (8)$$

$$\mathrm{Ag}\ (h^{+}) + OH^{-} \rightarrow \mathrm{Ag} + {}^{\bullet}OH \qquad (9)$$

3.2.2.3 The concentration of hydroxyl radicals

The concentration of hydroxyl radicals, which are considered a major reactive species in dye degradation, was monitored by the terephthalic acid photoluminescence probing technique. Terephthalic acid is non-fluorescent; however, it can react with hydroxyl radicals to give fluorescent 2-hydroxyterephthalic acid. On careful examination of Fig. 15, one can notice that terephthalic acid, being non-fluorescent, does not give any peak, while a pronounced peak appears at 423 nm for ZnAg3.

3.2.2.4 Photocatalytic degradation of MB under visible light:

The photocatalytic reactivity of the samples under a xenon lamp of 100 W intensity and with a cutoff filter to remove UV radiation ($\lambda \leq 420$ nm) was studied to investigate the role of metallic silver nanoparticles in shifting the photocatalytic response to the visible region. The results reveal that MB degradation increased from 28% to 76% on incorporation of 3 wt% Ag^0 on the ZnO surface during 2 h of irradiation (Fig. 16).

4. Conclusion

ZnO nanoparticles containing various proportions of metallic silver were prepared by an innovative combined sol-gel and chemical reduction method. Chitosan was used as an environmentally benign reducing agent to avoid the toxicity of traditionally used reducing agents. XPS and XRD analyses revealed the existence of metallic silver nanoparticles on the ZnO surface. Photoluminescence and XPS studies provided evidence for strong interaction between ZnO and Ag^0. The photocatalytic degradation of MB increases with increasing silver content up to 3 wt%, followed by reduction for the sample containing 5 wt% Ag. The ease of electron transfer between CB electrons of ZnO and the Fermi level of metallic silver nanoparticles, which in turn limits electron-hole recombination, is the main cause of enhancement of the photodegradation of MB under UV and solar radiation.

References

1. E. Forgacs, T. Cserhati, G. Oros, **Removal of synthetic dyes from wastewaters: a review**. Environ. Int. 30(7) (2004) 953.

2. M.A. Ahmed*, Z.M. Abou-Gamra, A.M. Salem, **Photocatalytic degradation of methylene blue dye over novel spherical mesoporous Cr_2O_3/TiO_2 nanoparticles prepared by sol-gel using octadecylamine template,** J. Environ. Chem. Engin. 5 (2017) 4251–4261

3. M.A. Messih, M.A. Ahmed, A. Soltan, S.S. Anis, **Facile approach for homogeneous dispersion of metallic silver nanoparticles on the surface of mesoporous titania for photocatalytic degradation of methylene blue and indigo carmine dyes.** J. Photochem. Photobiol. A 335 (2017) 40.

4. A. Azam, F. Ahmed, N. Arshi, M. Chaman, A.H. Naqvi, **Formation and characterization of ZnO nanopowder synthesized by sol–gel method,** J. Alloys Compd. 496 (2010) 399.

5. M.M. Khan, S.A. Ansari, M.E. Khan, M.O. Ansari, B.K. Min, M.H. Cho, **Visible light-induced enhanced photoelectrochemical and photocatalytic studies of gold decorated SnO_2 nanostructures.** New J. Chem. 39(4) (2015) 2758.

6. J. Zhao, C. Chen, W. Ma, **Photocatalytic degradation of organic pollutants under visible light irradiation,** Top. Catal. 35(3–4) (2005) 269.

7. X. Zhang, Y. Wang, F. Hou, H. Li, Y. Yang, X. Zhang, Y. Wang, **Effects of Ag loading on structural and photocatalytic properties of flower-like ZnO microspheres**, Appl. Surf. Sci. 391(2017) 476.

8. N. Güy, M. Özacar, **The influence of noble metals on photocatalytic activity of ZnO for Congo red degradation,** Int. J. Hydrogen Energy, 41(44) (2016) 20100.

9. B. Pant, M. Park, H.Y. Kim, S.J. Park, **Ag-ZnO photocatalyst anchored on carbon nanofibers:** s**ynthesis, characterization, and photocatalytic activities,** Synth. Met. 220 (2016) 533.

10. O. Bechambi, M. Chalbi, W. Najjar, S. Sayadi, **Photocatalytic activity of ZnO doped with Ag on the degradation of endocrine disrupting under UV irradiation and the investigation of its antibacterial activity**, Appl. Surf. Sci. 347 (2015) 414.

11. S. Sohrabnezhad, A. Seifi, **The green synthesis of Ag/ZnO in montmorillonite with enhanced photocatalytic activity,** Appl. Surf. Sci. 386 (2016) 33.

12. S. Rehman, R. Ullah, A.M. Butt, N.D. Gohar, **Strategies of making TiO_2 and ZnO visible light active,** J. Hazard. Mater. 170(2) (2009) 560.

13. M.A. Ahmed, M.F. Abdel Messih, E.F. El-Sherbeny, Suzan F. El-Hafez, Aliaa M.M. Khalifa, **Synthesis of metallic silver nanoparticles decorated mesoporous**

SnO_2 for removal of methylene blue dye by coupling adsorption and photocatalytic processes, J. Photochem. Photobiol.. A. 346 (2017) 77-88

14. Y. Zhang, Q. Wang, J. Xu, S. Ma, **Synthesis of Pd/ZnO nanocomposites with high photocatalytic performance by a solvothermal method**. Appl. Surf. Sci. 258(24) (2012) 10104.

15. J. Yuan, E.S.G. Choo, X. Tang, Y. Sheng, J. Ding, J. Xue. **Synthesis of ZnO–Pt nanoflowers and their photocatalytic applications,** Nanotechnology 21(18) (2010) 185606.

16. M.N. Tahir, F. Natalio, M.A. Cambaz, M. Panthöfer, R. Branscheid, U. Kolb, W. Tremel, **Controlled synthesis of linear and branched Au@ZnO hybrid nanocrystals and their photocatalytic properties,** Nanoscale 5(20) (2013) 9944.

17. Z. Han, L. Ren, Z. Cui, C. Chen, H. Pan, J. Chen. **Ag/ZnO flower heterostructures as a visible-light driven photocatalyst via surface plasmon resonance,** Appl. Catal. B 126 (2012) 298.

18. T. Cai, L. Wang, Y. Liu, S. Zhang, W. Dong, H. Chen, X. Yi, J. Yuan, X. Xia, C. Liu, S. Luo, **Ag_3PO_4/Ti_3C_2 MXene interface materials as a Schottky catalyst with enhanced photocatalytic activities and anti-photocorrosion performance,** Appl. Catal. B 239 (2018) 545–554 19. T. Cai, Y. Liu, L. Wang, S. Zhang, W. Dong, H. Chen, J. Ma, C. Liu, S. Luo, **Ultrafine Ag@AgI nanoparticles on cube single-crystal Ag_3PO_4 (100): an all-day-active Z-Scheme photocatalyst for environmental purification,** J. Colloid Interface Sci. 533 (2019) 95–105.

20. T. Cai, Y. Liu, L. Wang, S. Zhang, Y. Zeng, J. Yuan, J. Ma, W. Dong, C. Liu, S. Luo, **Silver phosphate-based Z-Scheme photocatalytic system with superior sunlight photocatalytic activities and anti-photocorrosion performance**, Appl. Catal. B 208 (2017) 1–13.

21. C. Jaramillo-Páez, J. A. Navío, M. C. Hidalgo, **Silver-modified ZnO highly UV-photoactive**, J. Photochem. Photobiol. A 356 (2018) 112–122.

22. S.M. Lama, J.A. Queka, J.C. **Sin, Mechanistic investigation of visible light responsive Ag/ZnO micro/ nanoflowers for enhanced photocatalytic performance and antibacterial activity,** J. Photochem. Photobiol. A 353 (2018) 171–184.

23. S.A. Ansari, M.M. Khan, J. Lee, M.H. Cho. **Highly visible light active Ag@ ZnO nanocomposites synthesized by gel-combustion route.** Ind. Eng. Chem. Res. 20(4) (2014) 1602.

24. B. Chai, X. Wang, S. Cheng, H. Zhou, F. Zhang. **One-pot triethanolamine-assisted hydrothermal synthesis of Ag/ZnO heterostructure microspheres with enhanced photocatalytic activit**y. Ceram. Int. 40(1) (2014) 429.

25.S.M. Hosseini, I. Abdolhosseini Sarsari, P. Kameli, H. Salamati, **Effect of Ag doping on structural, optical, and photocatalytic properties of ZnO nanoparticles**, J. Alloys Compd. 640 (2015) 408-415.
26. B.M. Rajbongshi, A. Ramchiary, B.M. Jha, S.K. Samdarshi, **Synthesis and characterization of plasmonic visible active Ag/ZnO photocatalyst.** J. Mater. Sci. Mater. Electron. 25(7) (2014) 2969.

27. Y. Zhang, J. Xu, Q. Wang, Z. Pan, S. Ma, Q. Chen, **Preparation and properties of ZnO loaded with uniform Ag nanoparticles**. Mater. Res. Bull. 73 (2016) 119.

28. D. Wei, W. Qian. **Facile synthesis of Ag and Au nanoparticles utilizing chitosan as a mediator agent.** Colloids Surf. B 62(1) (2008) 136.

29. A. Dolgonos, T.O. Mason, K.R. Poeppelmeier, **Direct optical band gap measurement in polycrystalline semiconductors: a critical look at the Tauc method**. J. Solid State Chem. 240 (2016) 43.

30. K.S. Sing. **Reporting physisorption data for gas/solid systems with special reference to the determination of surface area and porosity (recommendations 1984).** Pure Appl. Chem. 57(4) (1985) 603.

31. V. Vaiano, M. Matarangolo, J.J. Murcia, H. Rojas, J.A. Navío, M.C. Hidalgo, **Enhanced photocatalytic removal of phenol from aqueous solutions using ZnO modified with Ag.** Appl. Catal. B 225 (2018) 197–206.

32. A. Phuruangrat, S. Siri, P. Wadbua, S. Thongtem, **Microwave-assisted synthesis, photocatalysis and antibacterial activity of Ag nanoparticles supported on ZnO flowers.** J. Phys. Chem. Solids 126 (2019) 170–177.

33. H. Liu, L. Zhong, S. Govindaraju, K. Yun, **ZnO rod decorated with Ag nanoparticles for enhanced photocatalytic degradation of methylene blue.** J. Phys. Chem. Solids,129 (2019) 46–53.

34. M.J. Sampaio, M.J. Lima, D.L. Baptista, A.M. Silva, C.G. Silva, J.L. Faria**, Ag-loaded ZnO materials for photocatalytic water treatment.** Chem. Eng. J. 318 (2017) 95.

35. J.C. Bian, F. Yang, Z. Li, J.L. Zeng, X.W. Zhang, Z.D. Chen, J. Wang, **Mechanisms in photoluminescence enhancement of ZnO nanorod arrays by the localized surface plasmons of Ag nanoparticles**. Appl. Surf. Sci. 258(22) (2012) 8548.

36. J. Kaur, K. Gupta, V. Kumar, S. Bansal, S. Singhal, **Synergic effect of Ag decoration onto ZnO nanoparticles for the remediation of synthetic dye wastewater**. Ceram. Int. 42(2) (2016) 2378.

37. L. Chen, J. Li, L. Yuan, Q. Cai. **Synthesis and photocatalytic application of Au/Ag nanoparticle-sensitized ZnO films**. Appl. Surf. Sci. 273 (2013) 82.

38. E. Mendoza-Mendoza, A.G. Nuñez-Briones, L.A. García-Cerda, R.D. Peralta-Rodríguez, A.J. Montes-Luna, **One-step synthesis of ZnO and Ag/ZnO heterostructures and their photocatalytic activity,** Ceram. Int. 44 (2018) 6176–6180.

39. A.N. Kadam, D.P. Bhopate, V.V. Kondalkar, S.M. Majhi, S.-W. Lee, **Facile synthesis of Ag-ZnO core–shell nanostructures with enhanced photocatalytic activity,** J. Ind. Eng. Chem. 61 (2018) 78–86.

40. M. Wang, J. Xu, T. Sun, Y. Tang, G. Jiang, Y. Shi, **Facile photochemical synthesis of hierarchical cake-like ZnO/Ag composites with enhanced visible-light photocatalytic activities,** Mater. Lett. 219 (2018) 236–239.

41. S.M. Lama, J.A. Queka, J.C. **Sin, Mechanistic investigation of visible light responsive Ag/ZnO micro/nanoflowers for enhanced photocatalytic performance and antibacterial activity,** J. Photochem. Photobiol. A 353 (2018) 171–184.

42. S. Rajaboopathi, S. Thambidura, **Enhanced photocatalytic activity of Ag-ZnO nanoparticles synthesized by using Padina gymnospora seaweed extract**, J. Mol. Liq. 262 (2018) 148–160.

43. M. Kang, S.J. Choung, J.Y. Park, **Photocatalytic performance of nanometer-sized FexOy/TiO2 particle synthesized by hydrothermal method**, Catal. Today 87 (2003) 87–97.

44. Karakitsou, K. E., & Verykios, X. E. (1993). Effects of altervalent cation doping of titania on its performance as a photocatalyst for water cleavage. *The Journal of Physical Chemistry*, *97*(6), 1184-1189.

45. Dung, N. T., Van Khoa, N., & Herrmann, J. M. (2005). **Photocatalytic degradation of reactive dye RED-3BA in aqueous TiO_2 suspension under UV-visible light.** International Journal of photoenergy, *7*(1), 11-15.

46. X. Chen, Z. Wu, D. Liu, Z. Gao, **Preparation of ZnO Photocatalyst for the efficient and rapid photocatalytic degradation of azo dye,** Nanoscale Res. Lett. 12 (2017) 143.

47. D. Zhang, X. Pu, H. Li, Y. Moon Yu, J.J Shim, P. Cai, S. Kim, H.J. Seo, **Microwave-assisted combustion synthesis of Ag/ZnO nanocomposites and their photocatalytic activities under ultraviolet and visible-light irradiation,** Mater. Res. Bull. 61 (2015) 321–325.

48. Y.W. Tseng, F.Y. Hung, T. S. Lui, S.J. Chang, **Structural and Raman properties of silver-doped ZnO nanorod arrays using electrically induced crystallization process,** Mater. Res. Bull. 64 (2015) 274–278.

49. M.H. Sarvari, T.H. Kachouei, F. Moeini, **A novel and active catalyst Ag/ZnO for oxidant-free dehydrogenation of alcohols,** Mater. Res. Bull. 72 (2015) 98–105.

Fig. 1. The proposed mechanism for reduction of silver ions by chitosan.

Fig. 2. The photocatalytic reactor used in the study of the photocatalytic activity of the samples.

Fig. 3. X-ray diffraction patterns of ZnO and various Ag/ZnO powders.

Fig. 4. High-resolution transmission electron microscopy images of ZnO (a), ZnAg1 (b), ZnAg3 (c), and ZnAg5 (d), and lattice spacing of ZnAg3 (e).

Fig. 5. N_2 adsorption–desorption isotherms of ZnO (a), ZnAg1 (b), ZnAg3 (c), and ZnAg5 (d).

Fig. 6. X-ray photoelectron spectroscopy core level spectra of Zn 2p (a), O 1s (b), and Ag 3d (c) regions for ZnAg5.

Fig. 7. Absorption spectra of pure and Ag-doped ZnO powdered samples.

Fig. 8. $(Ah\nu)^2$ versus photon energy ($h\nu$) for pure and Ag-doped ZnO samples.

Fig. 9. Photoluminescence spectra of pure ZnO and ZnAg3.

Fig. 10. Photocatalytic degradation of methylene blue over ZnO (a), ZnAg1 (b), ZnAg3 (c), and ZnAg5 (d).

Fig. 11. Pseudo-first-order kinetics of methylene blue degradation over ZnO, ZnAg1, ZnAg3, and ZnAg5.

Fig. 12. Photocatalytic degradation of methylene blue over ZnAg3 under solar irradiation.

Fig. 13. Ag/ZnO photocatalytic mechanism under UV light. CB, conduction band; VB valence band.

Fig. 14. Ag/ZnO photocatalytic mechanism under sunlight. CB, conduction band; VB valence band.

Fig. 15. Fluorescence spectral changes observed during illumination of ZnAg3 in 5×10^{-5} M NaOH solution of terephthalic acid (excitation at 315 nm).

Fig. 16. Photocatalytic degradation of methylene blue over ZnO and ZnAg3 under a halogen lamp.

Table 1. The crystallite size, surface area, pore volume, and pore diameter of pure and Ag-doped ZnO nanocrystalline powders.

Ag (wt%)	Crystallite size	Surface	Pore	Pore diameter

	(nm)	area(m^2/g)	volume(ml/g)	
0	61	7.8	0.039	17.6
1	61	6.5	0.036	16.3
3	53.6	5.2	0.034	15.8
5	47.5	4.7	0.033	15.4

Table 2. Band gap energy and the corresponding absorption edge of the samples.

Ag (wt%)	E_g (eV)	Absorption edge (nm)
0	3.22	385
1	3.22	385
3	3.18	389.9
5	3.18	389.9

Table 3. Catalytic parameters for each photocatalyst.

Sample	Ag (wt%)	Photocatalytic activity of sample for MB degradation (%)	Moles of MB converted	TOR (removed mol $_{MB}$/g $_{catalyst}$ min)
ZnO	0	65.6	1.312×10^{-5}	5.46×10^{-7}
ZnAg1	1	79.5	1.59×10^{-5}	6.62×10^{-7}
ZnAg3	3	82.6	1.652×10^{-5}	6.88×10^{-7}
ZnAg5	5	81.2	1.624×10^{-5}	6.76×10^{-7}

MB, methylene blue; TOR turnover rate.

Table 4. Kinetic parameters for methylene blue photocatalytic degradation by each photocatalyst.

Sample	*k* (min^{-1})	$t_{1/2}$ (min)
ZnO	0.0043	161.2
ZnAg1	0.0067	103.5
ZnAg3	0.007	99

ZnAg5	0.0068	102

Caption to figures

Fig. 1 The proposed mechanism for reducing silver ions by chitosan

Fig. 2 Schematic illustration of the photocatalytic reactor used in testing the prepared samples photocatalytic activity.

Fig. 3 XRD patterns of ZnO and various Ag/ZnO powders.

Fig. 4 HRTEM images of ZnO (a), ZnAg1 (b), ZnAg3 (c), and ZnAg5 (d).

Fig. 5 N_2 adsorption–desorption isotherms of ZnO (a), ZnAg1 (b), ZnAg3 (c), and ZnAg5 (d).

Fig. 6 XPS patterns of ZnAg5

Fig. 7 The absorption spectra for pure and Ag doped ZnO powdered samples

Fig. 8 $(Ah\nu)^2$ vs. photon energy (hν) plots for pure and silver doped ZnO samples.

Fig. 9 PL spectra for pure and 3 wt. % Ag doped ZnO.

Fig. 10 Photocatalytic degradation of methylene blue over ZnO (a), ZnAg1 (b), ZnAg3 (c), and ZnAg5 (d).

Fig. 11 The pseudo first order kinetics of methylene blue degradation over ZnO, ZnAg1, ZnAg3 and ZnAg5.

Fig. 12 Photocatalytic degradation of methylene blue over ZnAg3 under solar irradiation.

Fig. 13 Fluorescence spectral changes observed during illumination of ZnAg3 in 5 x 10^{-5} M NaOH solution of terephthalic acid (excitation at 315 nm).

Fig. 14 Photocatalytic degradation of MB dye over ZnO and ZnAg3 under halogen lamp

Fig. 15 Schematic of Ag/ZnO photocatalytic mechanism under UV light.

Fig.16 Schematic of Ag/ZnO photocatalytic mechanism under sun light.

Fig. 1

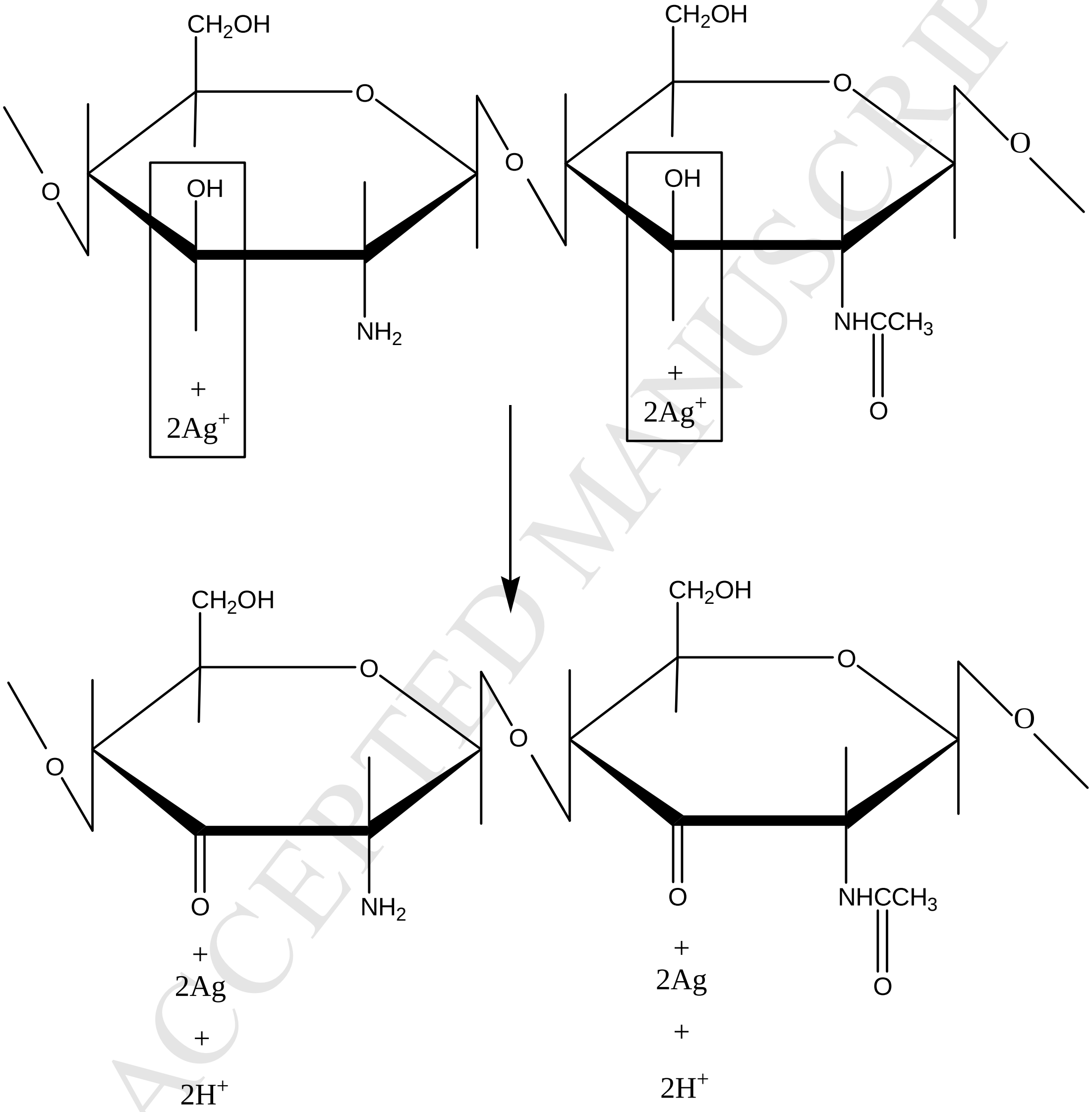

Fig.2

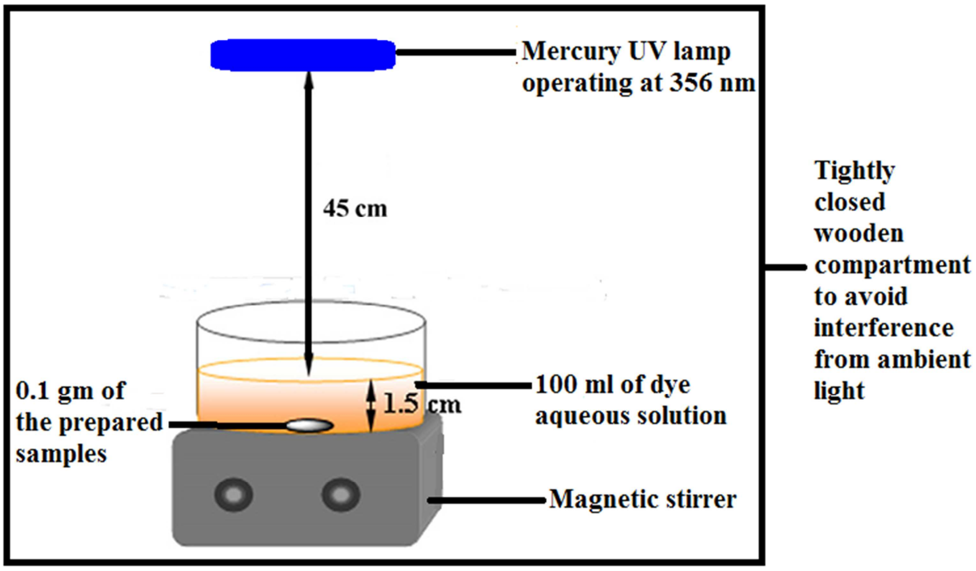
Mercury UV lamp
operating at 356 nm
45 cm
Tightly closed wooden compartment to avoid interference from ambient light
0.1 gm of the prepared samples
1.5 cm
100 ml of dye aqueous solution
Magnetic stirrer

Fig.3

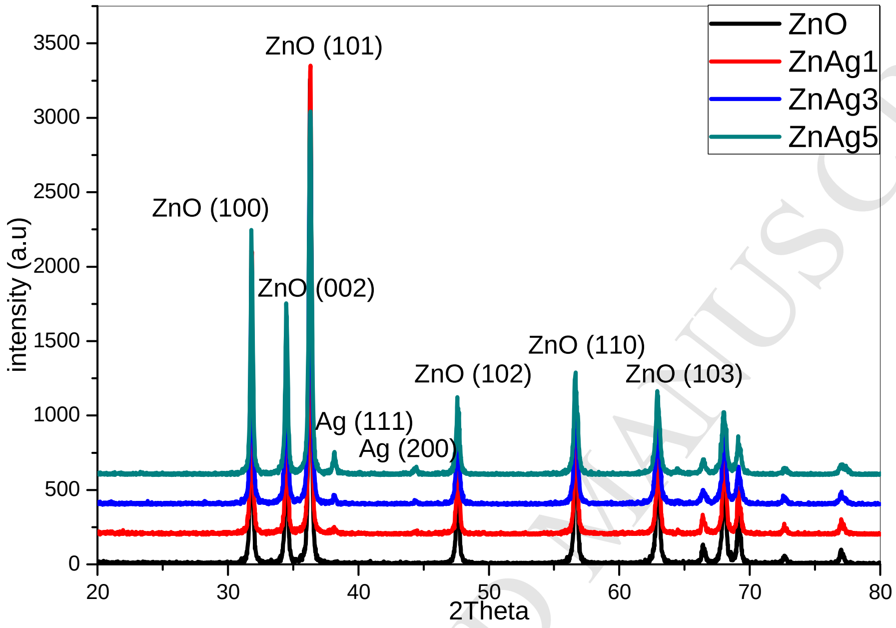
intensity (a.u)
0
500
1000
1500
2000
2500
3000
3500
20
30
40
50
60
70
80
2Theta
ZnO (101)
ZnO (100)
ZnO (002)
Ag (111)
Ag (200)
ZnO (102)
ZnO (110)
ZnO (103)
ZnO
ZnAg1
ZnAg3
ZnAg5

Fig. 4

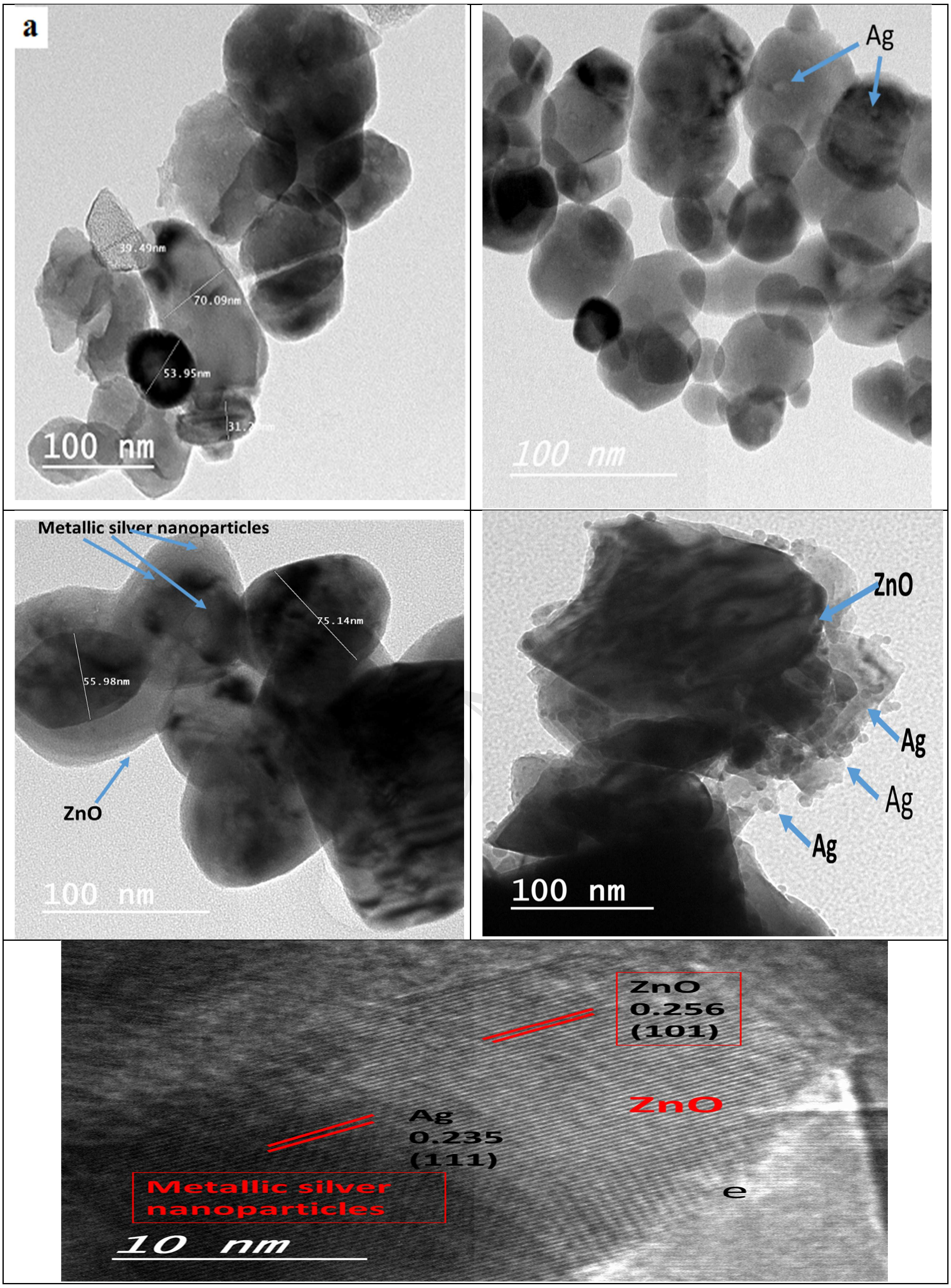
a
39.49nm
70.09nm
53.95nm
31.2
100 nm
Ag
100 nm
Metallic silver nanoparticles
75.14nm
55.98nm
ZnO
100 nm
ZnO
Ag
Ag
Ag
100 nm
ZnO 0.256 (101)
ZnO
Ag 0.235 (111)
Metallic silver nanoparticles
e
10 nm

Fig. 5

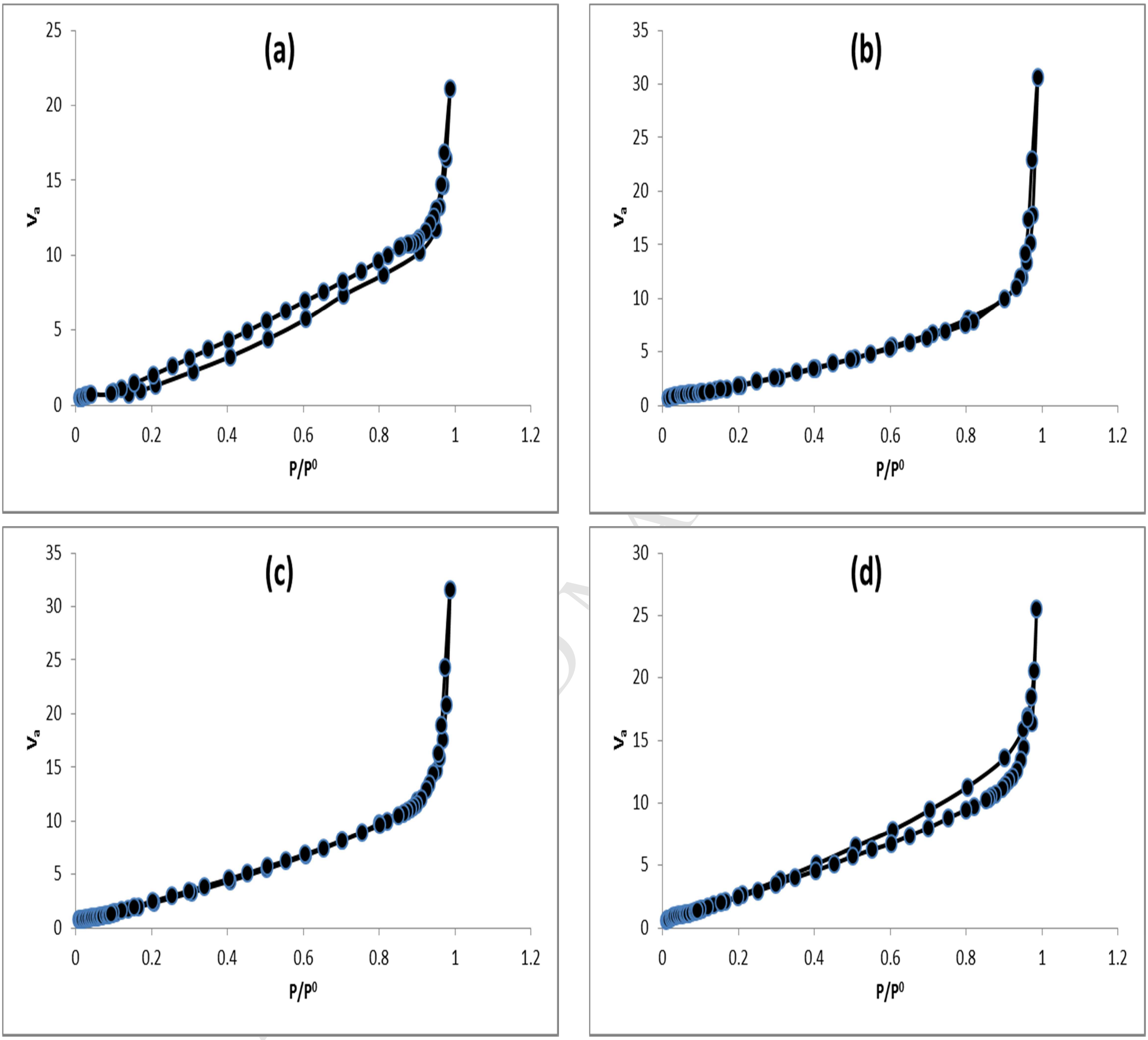

Fig. 6

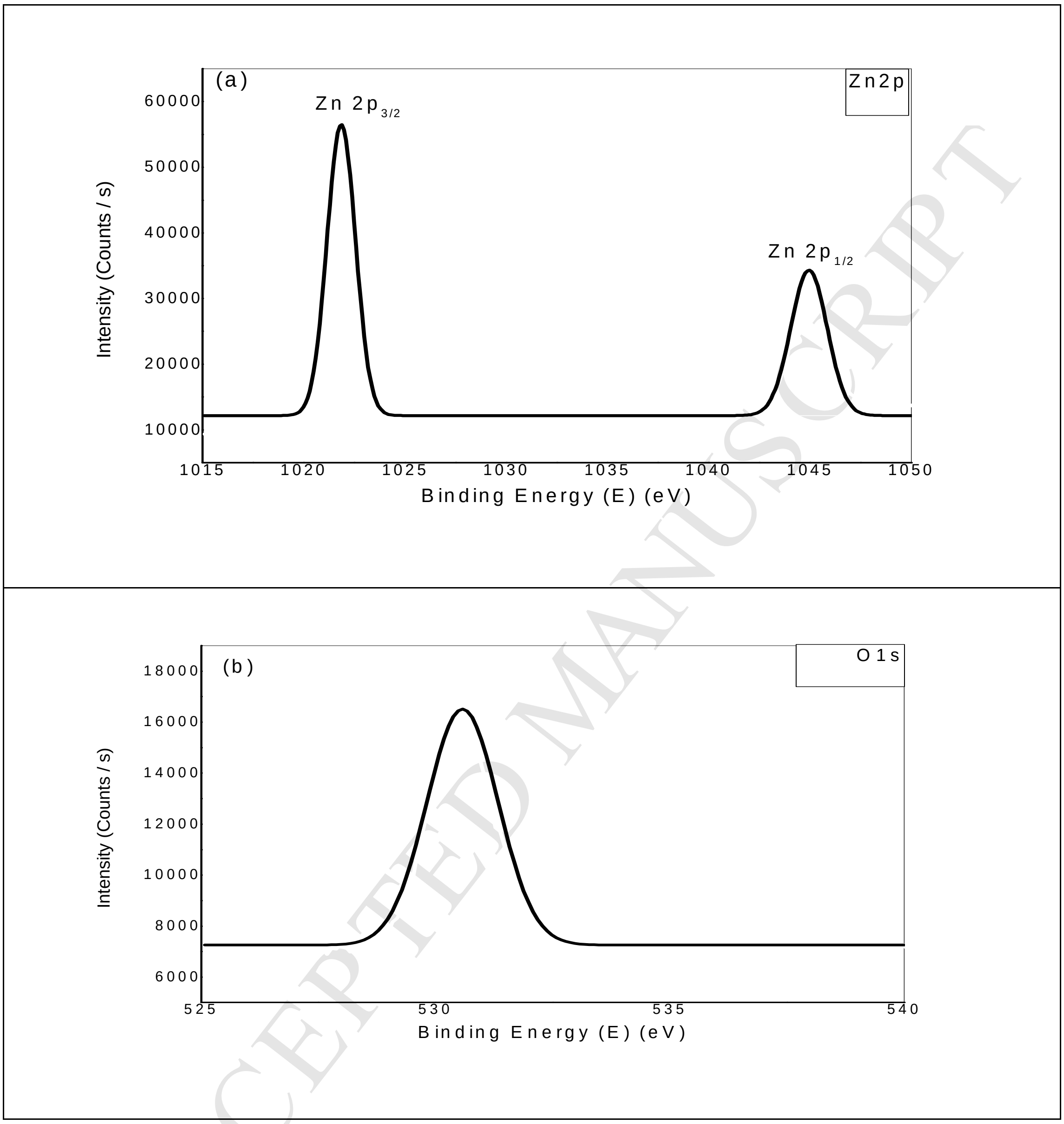
(a)
Zn2p
Zn 2p3/2
Zn 2p1/2
Intensity (Counts / s)
60000
50000
40000
30000
20000
10000
1015
1020
1025
1030
1035
1040
1045
1050
Binding Energy (E) (eV)
(b)
O 1s
Intensity (Counts / s)
18000
16000
14000
12000
10000
8000
6000
525
530
535
540
Binding Energy (E) (eV)

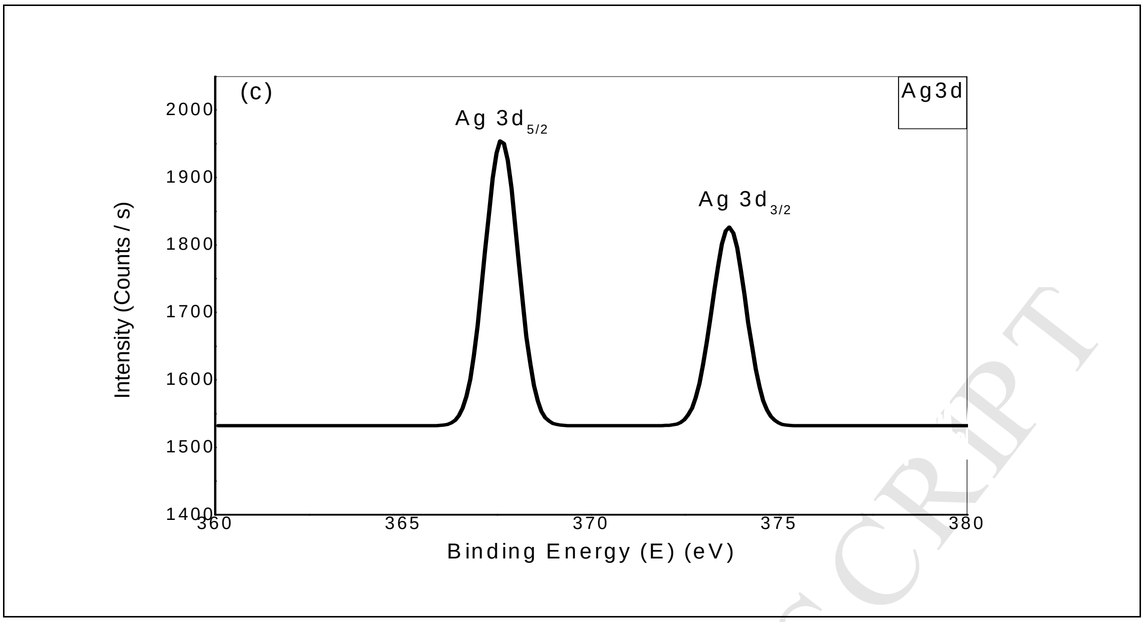

Fig. XPS core level spectra of Zn 2p (a), O 1s (b) and Ag 3d (c) regions for ZnAg5 sample.

Fig. 7

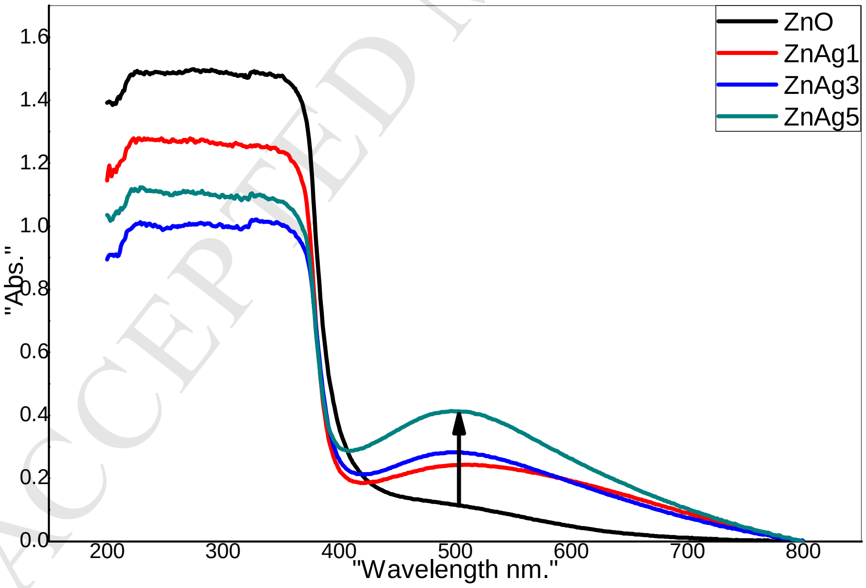

Fig. 8

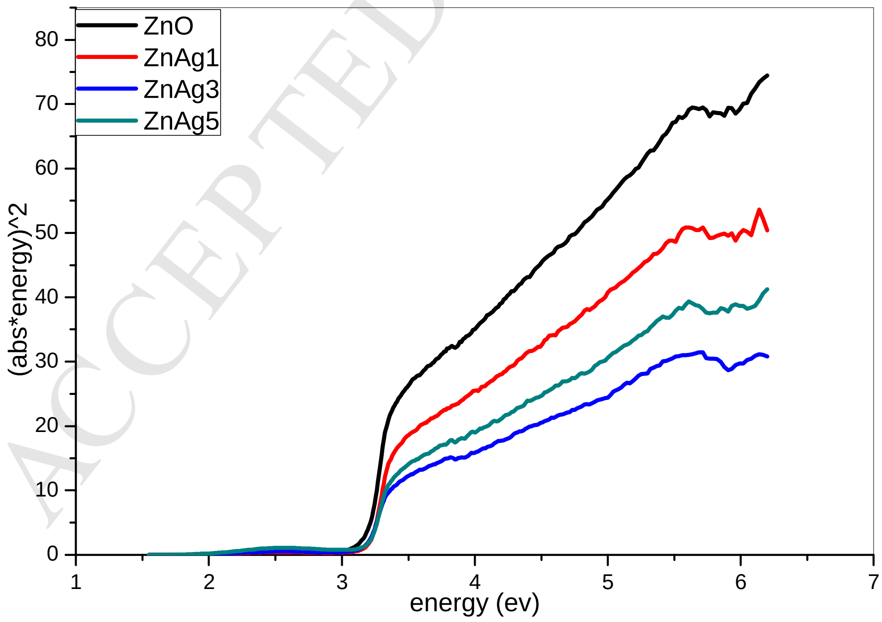
ZnO
ZnAg1
ZnAg3
ZnAg5
(abs*energy)^2
0
10
20
30
40
50
60
70
80
1
2
3
4
5
6
7
energy (ev)

Fig. 9

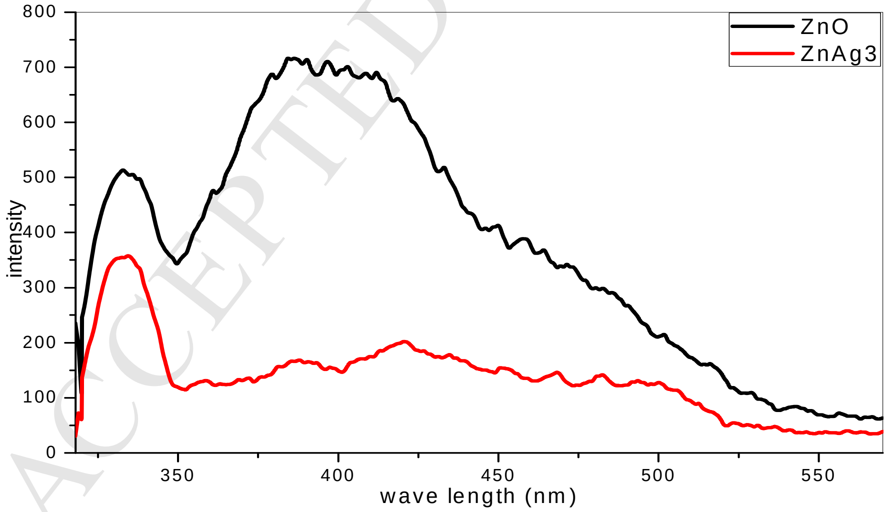
800
700
600
500
400
300
200
100
0
intensity
350
400
450
500
550
wave length (nm)
ZnO
ZnAg3

Fig. 10

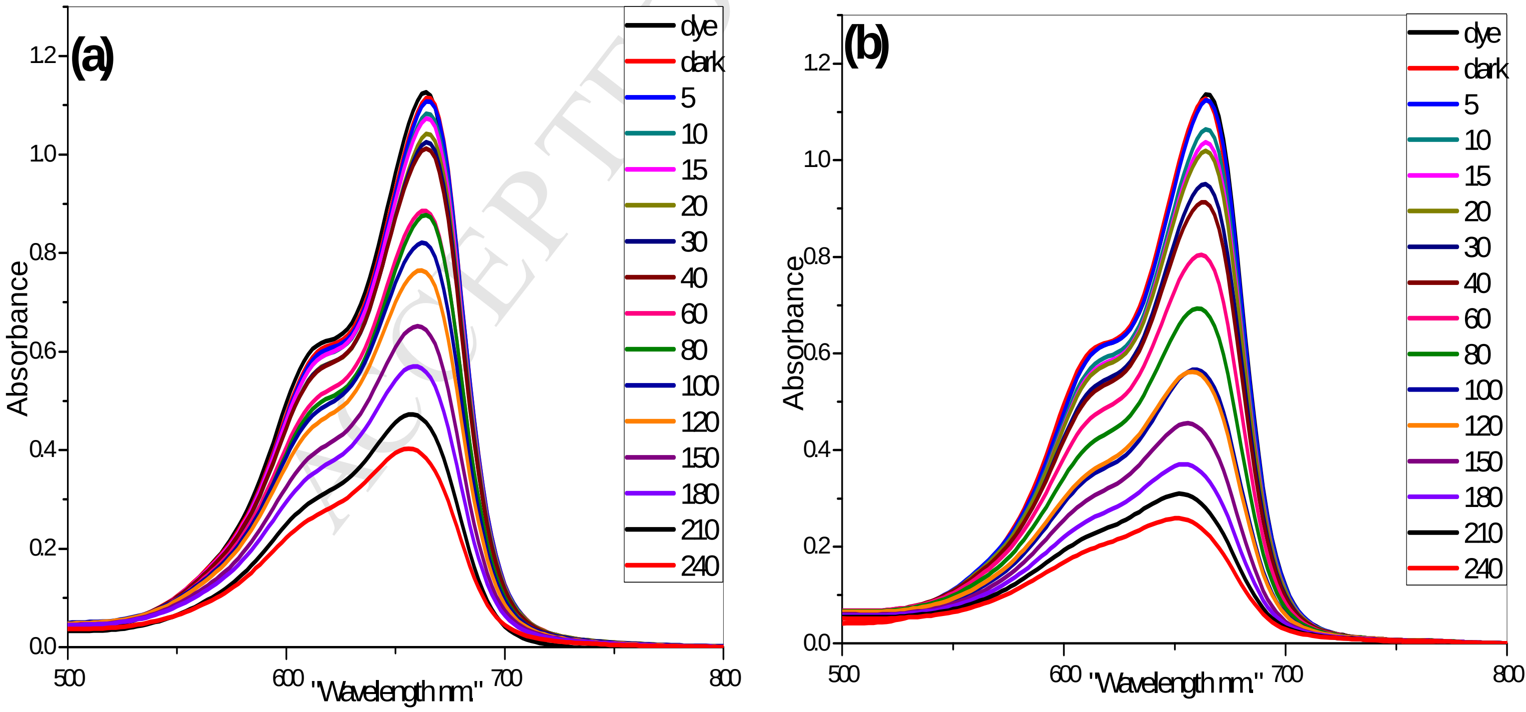
(a)
(b)
Absorbance
"Wavelength nm"
0.0
0.2
0.4
0.6
0.8
1.0
1.2
500
600
700
800
dye
dark
5
10
15
20
30
40
60
80
100
120
150
180
210
240

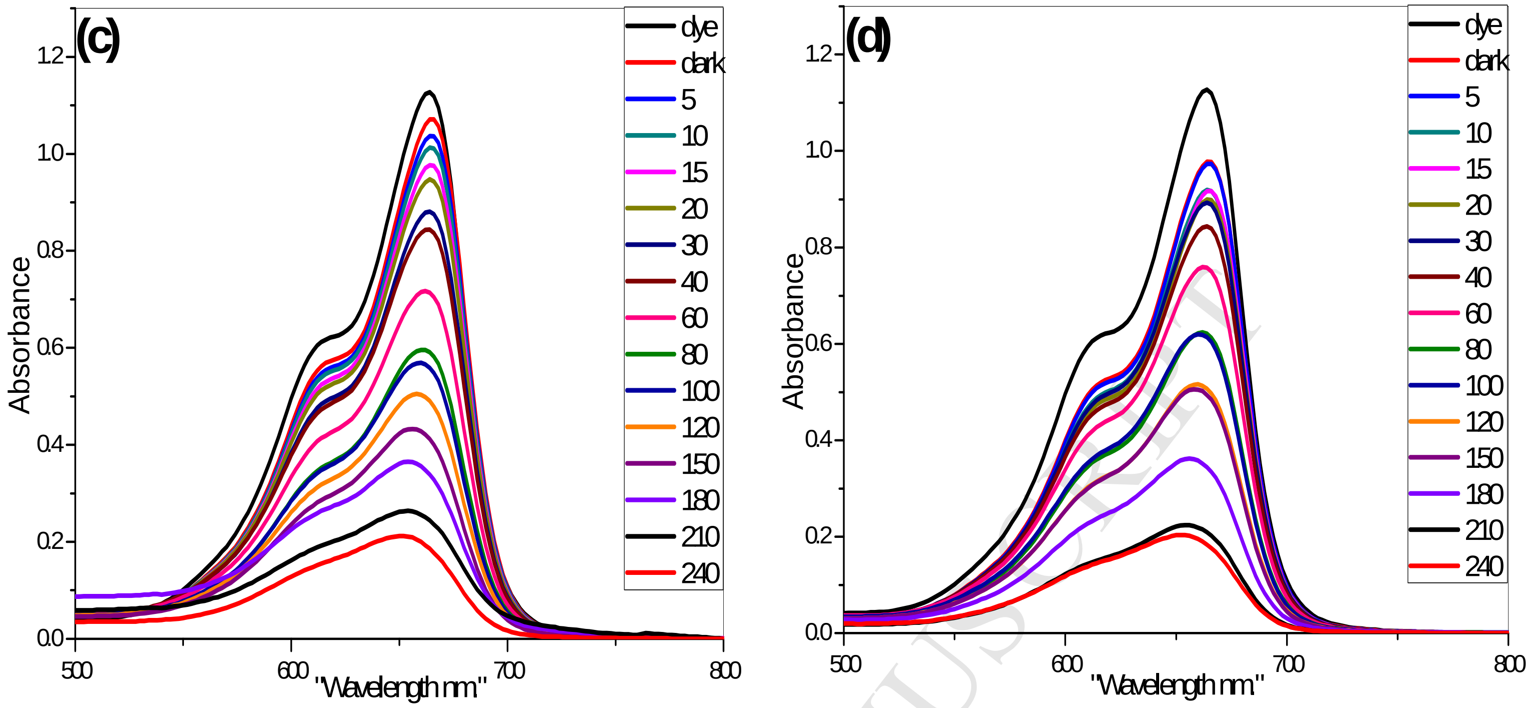
(c)
(d)
Absorbance
"Wavelength nm"
0.0
0.2
0.4
0.6
0.8
1.0
1.2
500
600
700
800
dye
dark
5
10
15
20
30
40
60
80
100
120
150
180
210
240

Fig. 11

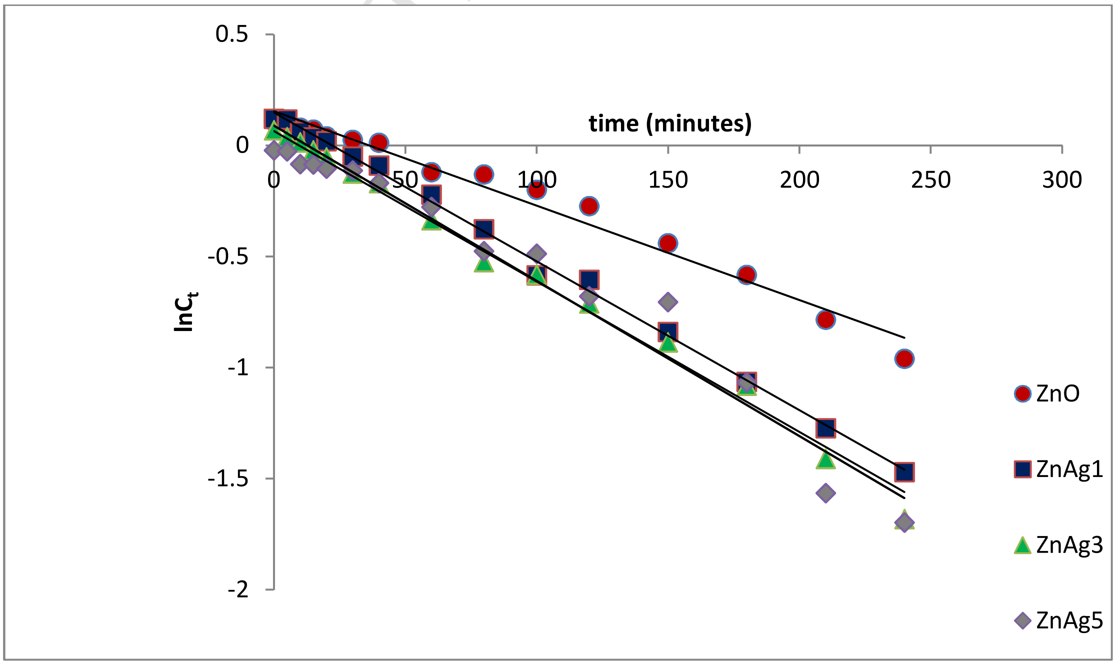
time (minutes)
lnC_t
0.5
0
-0.5
-1
-1.5
-2
0
50
100
150
200
250
300
ZnO
ZnAg1
ZnAg3
ZnAg5

Fig. 12

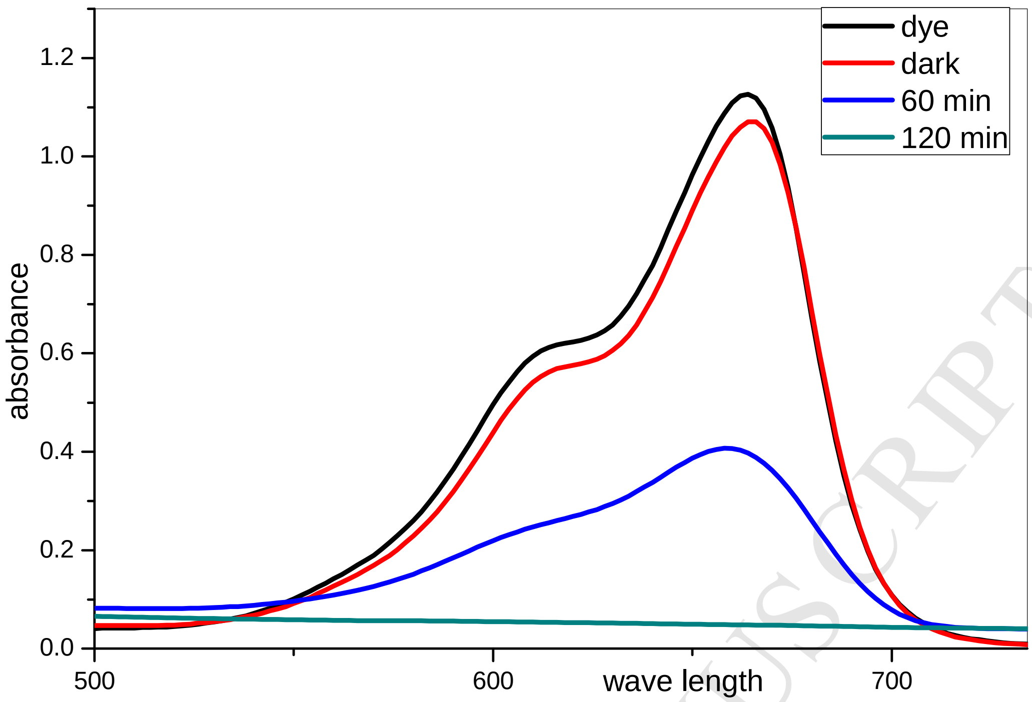
dye
dark
60 min
120 min
absorbance
0.0
0.2
0.4
0.6
0.8
1.0
1.2
500
600
700
wave length

Fig. 13

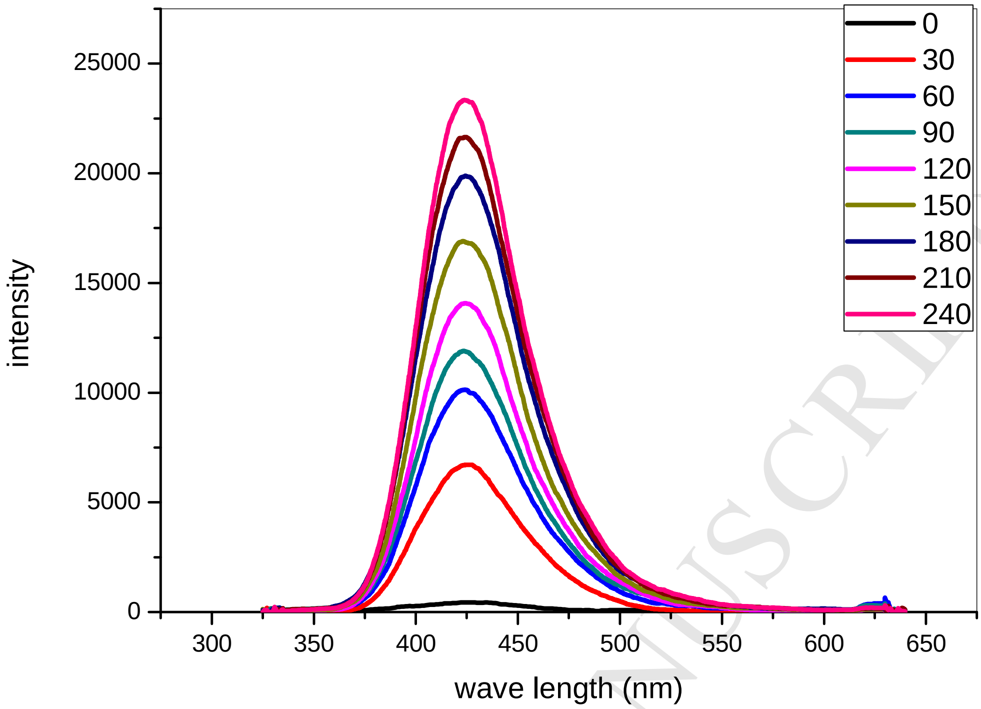
intensity
25000
20000
15000
10000
5000
0
300
350
400
450
500
550
600
650
wave length (nm)
0
30
60
90
120
150
180
210
240

Fig. 14

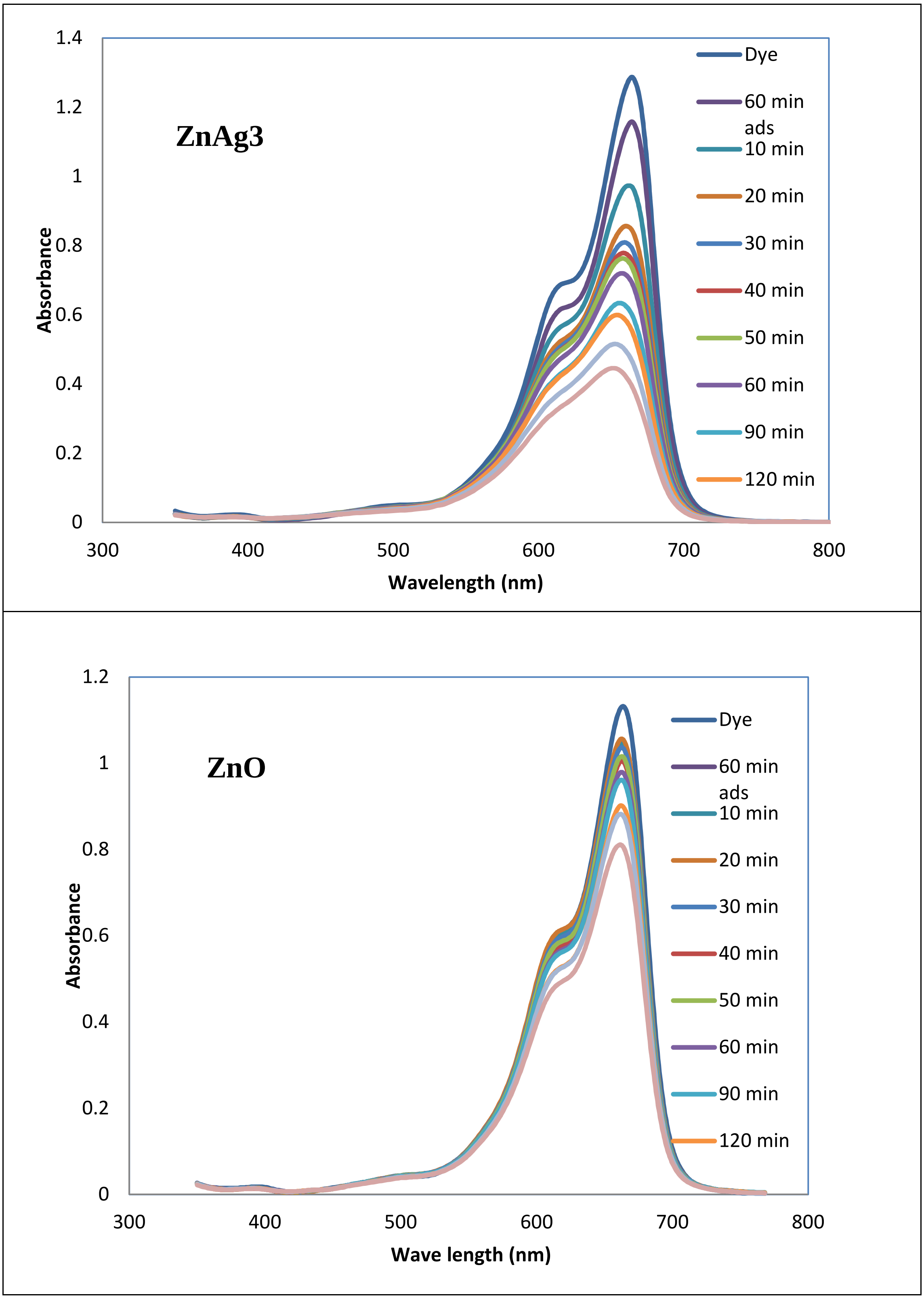
ZnAg3
Absorbance
1.4
1.2
1
0.8
0.6
0.4
0.2
0
300
400
500
600
700
800
Wavelength (nm)
Dye
60 min ads
10 min
20 min
30 min
40 min
50 min
60 min
90 min
120 min
ZnO
Absorbance
1.2
1
0.8
0.6
0.4
0.2
0
300
400
500
600
700
800
Wave length (nm)
Dye
60 min ads
10 min
20 min
30 min
40 min
50 min
60 min
90 min
120 min

Fig. 15

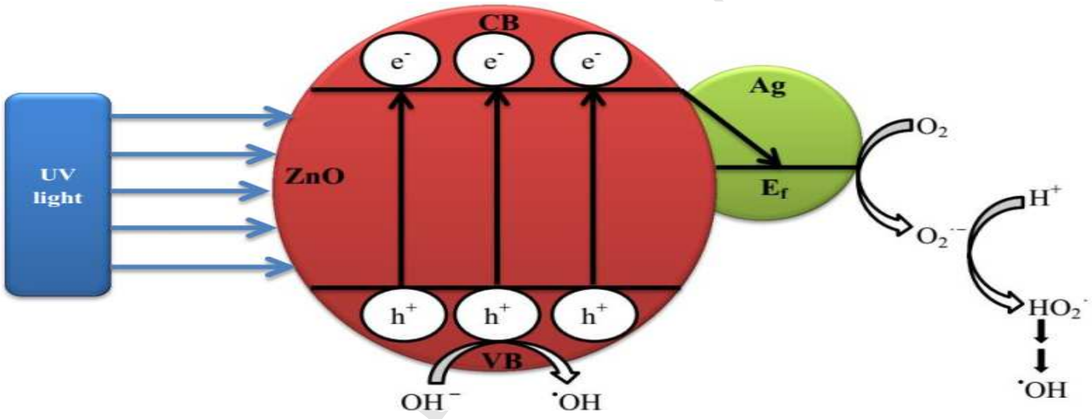

Fig.16

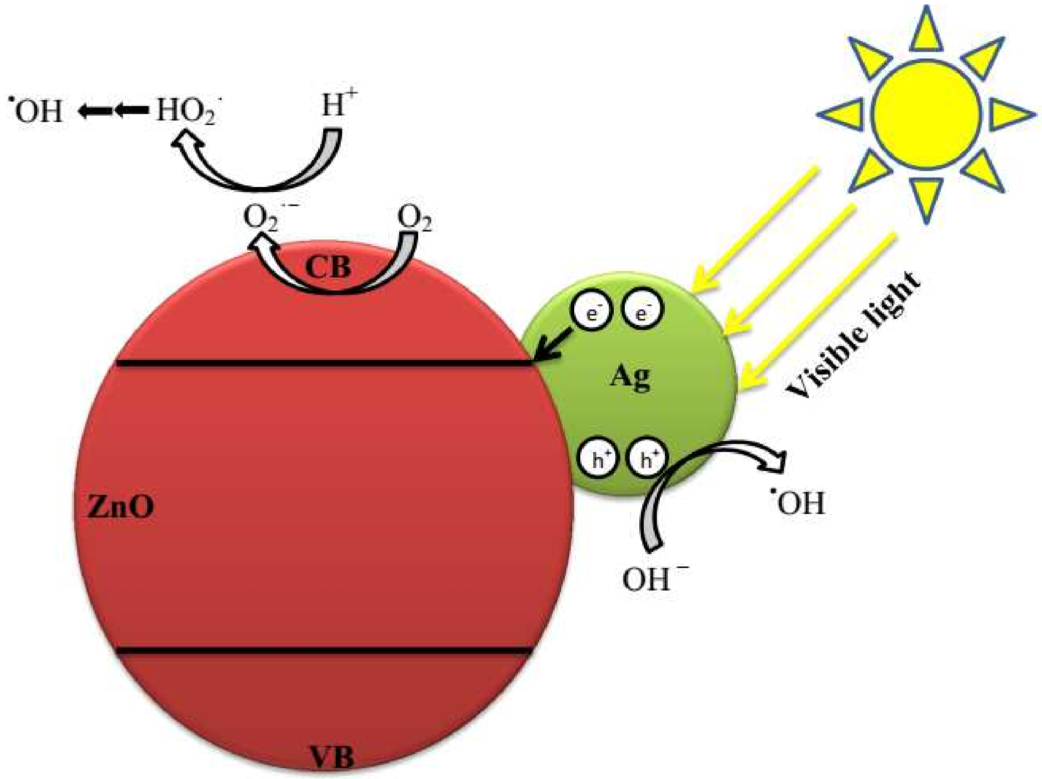

Caption to tables

Table 1. The crystallite size of pure and Ag doped ZnO nanocrystalline powders.

Ag wt. %	crystallite size (nm)
0	61
1	61
3	53.6
5	47.5

Table 2. Band gap energy and the corresponding absorption edge of the prepared samples.

Ag wt.%	E_g (eV)	absorption edge (nm)
0	3.22	385
1	3.22	385
3	3.18	389.9
5	3.18	389.9

Table 3. Catalytic parameters for each photocatalyst

sample	Ag wt.%	Photocatalytic activity of each sample for MB degradation %	Moles converted of MB	TOR (removed $mol_{MB}/g_{cat}.min$)
ZnO	0	65.6	1.312×10^{-5}	5.46×10^{-7}
ZnAg1	1	79.5	1.59×10^{-5}	6.62×10^{-7}
ZnAg3	3	82.6	1.652×10^{-5}	6.88×10^{-7}
ZnAg5	5	81.2	1.624×10^{-5}	6.76×10^{-7}

Table 4. Kinetic parameters for MB photocatalytic degradation by each photocatalyst.

sample	K ($minute^{-1}$)	$t_{1/2}$ (minute)
ZnO	0.0043	161.2
ZnAg1	0.0067	103.5
ZnAg3	0.007	99
ZnAg5	0.0068	102

Highlights

- Ag/ZnO nanoparticles were synthesized by the sol-gel route.
- Chitosan facilitates reduction of silver ions to metallic silver nanoparticles.
- The photocatalytic degradation of methylene blue increases with increasing silver content up to 3 wt%.
- XPS revealing the existence of Zn and Ag^0